Determination of optical scattering properties of highly-scattering media in optical coherence tomography images

David Levitz, Lars Thrane, Michael H. Frosz, and Peter E. Andersen

Optics and Fluid Dynamics Department, Risø National Laboratory, P.O. Box 49, DK-4000 Roskilde, Denmark
david.levitz@risoe.dk, lars.thrane@risoe.dk, michael.h.frosz@risoe.dk, peter.andersen@risoe.dk

Claus B. Andersen

Department of Pathology, Rigshospitalet, Telium Bygning, Frederick V's Vej, DK-2100 København Ø, Denmark
clausbrh01871andersen@rh.dk

Jurga Valanciunaite, Johannes Swartling, and Stefan Andersson-Engels

Department of Physics, Lund Institute of Technology, P.O. Box 118, SE-221 00 Lund, Sweden
jurgaval@centras.lt, johannes.swartling@polimi.it, stefan.andersson-engels@fysik.lth.se

Peter R. Hansen

Department of Cardiology, Amtssygehuset i Gentofte, Niels Andersensvej 65, DK-2900 Hellerup, Denmark
peha@gentoftehosp.kbhamt.dk

Abstract: We developed a new algorithm that fits optical coherence tomography (OCT) signals as a function of depth to a general theoretical OCT model which takes into account multiple scattering effects. With use of this algorithm, it was possible to extract both the scattering coefficient and anisotropy factor from a particular region of interest in an OCT image. The extraction algorithm was evaluated against measurements from an integrating sphere on a set of tissue phantoms and yielded valid results. Finally, a preliminary *ex vivo* OCT investigation on human aortic specimen indicated that the algorithm may contribute importantly to differentiation between normal and atherosclerotic arteries. We conclude that this algorithm may facilitate tissue characterization by OCT.

OCIS codes: (170.4500) optical coherence tomography, (290.0290) scattering, (170.4580) optical diagnostics for medicine

References and Links

1. C. F. Bohren and D. R. Huffman, *Absorption and scattering of light by small particles* (John Wiley & Sons, Inc., New York, NY 1983).
2. Z. Fayad and V. Fuster, "Clinical imaging of the high-risk or vulnerable atherosclerotic plaque," Circ. Res. **89,** 305-316 (2001).
3. J. C. Kennedy, R. H. Pottier, and D. C. Pross, "Photodynamic therapy with endogenous protoporphyrin IX: Basic principles and present clinical experience," J. Photochem. Photobiol. B **6,** 143-148 (1990).
4. D. Huang, E. A. Swanson, C. P. Lin, J. S. Schuman, W. G. Stinson, W. Chang, M. R. Hee, T. Flotte, K. Gregory, C. A. Puliafito, and J. G. Fujimoto, "Optical coherence tomography," Science **254,** 1178-1181 (1991).
5. B. Povazay, K. Bizheva, A. Unterhuber, B. Hermann, H. Sattmann, A. F. Fercher, W. Drexler, A. Apolonski, W. J. Wadsworth, J. C. Knight, P. S. J. Russel, M. Vetterlein, and E. Scherzer, "Submicrometer axial resolution optical coherence tomography," Opt. Lett. **27,** 1800-1802 (2002).
6. G. J. Tearney, S. A. Boppart, B. Bouma, M. E. Brezinski, N. J. Weissman, J. F. Southern, and J. G. Fujimoto, "Scanning single-mode fiber optic catheter-endoscope for optical coherence tomography," Opt. Lett. **21,** 543-545 (1996).

#3365 - $15.00 US Received 14 November 2003; revised 30 December 2003; accepted 8 January 2004

7. J. M. Schmitt, A. Knüttel, M. Yadlowsky, and M. A. Eckhaus, "Optical-coherence tomography of a dense tissue: statistics of attenuation and backscattering," Phys. Med. Biol. **39,** 1705-1720 (1994).
8. N. M. Shakhova, V. M. Gelikonov, V. A. Kamensky, R. V. Kuranov, and E. V. Turchin, "Clinical aspects of the endoscopic optical coherence tomography: a methods for improving the diagnostics efficiency," Laser Physics **12,** 23-32 (2002).
9. D. Levitz, C. B. Andersen, M. H. Frosz, L. Thrane, P. R. Hansen, T. M. Jørgensen, and P. E. Andersen "Assessing blood vessel abnormality via extracting scattering properties from OCT images" in *European Conference in Biomedical Optics (ECBO)*, W. Drexler, ed. Proc. SPIE **5140**, 12-19 (2003).
10. R. O. Esenaliev, K. V. Larin, I. V. Larina, and M. Motamedi, "Noninvasive monitoring of glucose concentration with optical coherence tomography," Opt. Lett. **26,** 992-994 (2001).
11. L. Thrane, H. T. Yura, and P. E. Andersen, "Analysis of optical coherence tomography systems based on the extended Huygens-Fresnel principle," J. Opt. Soc. Am. A **17,** 484-490 (2000).
12. G. J. Tearney, B. Bouma, and J. G. Fujimoto, "High-speed phase- and group-delay scanning with a grating-based phase control delay line," Opt. Lett. **22,** 1811-1813 (1997).
13. A. M. Rollins and J. A. Izatt, "Optimal interferometer designs for optical coherence tomography," Opt. Lett. **24,** 1484-1486 (1999).
14. R. F. Lutomirski and H. T. Yura, "Propagation of a finite optical beam in an inhomogeneous medium," Appl. Opt. **10,** 1652-1658 (1971).
15. A. E. Siegman, *Lasers* (University Science Books, Mill Valley, CA 1986).
16. H. T. Yura, L. Thrane, and P. E. Andersen, "Closed form solution for the Wigner phase-space distribution function for diffuse reflection and small angle scattering in a random medium," J. Opt. Soc. Am. A **17,** 2464-2474 (2000).
17. C. C. Cheng and M. G. Raymer, "Propagation of transverse optical coherence in random multiple-scattering media," Phys. Rev. A **62,** 1-12 (2000).
18. S. A. Prahl, Inverse Adding-Doubling Software. 1999. http://omlc.ogi.edu/software/iad/index.html
19. J. Swartling, J. S. Dam, and S. Andersson-Engels, "Comparison of spatially and temporally resolved diffuse-reflectance measurement systems for determination of biomedical optical properties," Appl. Opt. **42,** 4612-4620 (2003).
20. D. D. Royston, R. S. Poston, and S. A. Prahl, "Optical properties of scattering and absorbing materials used in the development of optical phantoms at 1064 nm," J. Biomed. Opt. **1,** 110-116 (1997).
21. I. K. Jang, B. E. Bouma, D. H. Kang, S. J. Park, S. W. Park, K. B. Seung, K. B. Choi, M. Shishkov, K. H. Schlendorf, E. Pomerantsev, S. L. Houser, H. T. Aretz, and G. J. Tearney, "Visualization of coronary atherosclerotic plaques in patients using optical coherence tomography: comparison with intravascular ultrasound," J Am Coll Cardiol **39,** 604-609 (2002).
22. H. Yabushita, B. E. Bouma, S. L. Houser, H. T. Aretz, I. K. Jang, K. H. Schlendorf, C. R. Kauffman, M. Shishkov, D. H. Kang, E. F. Halpern, and G. J. Tearney, "Characterization of human atherosclerosis by optical coherence tomography," Circulation **106,** 1640-1645 (2002).
23. G. J. Tearney, H. Yabushita, S. L. Houser, H. T. Aretz, I. K. Jang, K. H. Schlendorf, C. R. Kauffman, M. Shishkov, E. F. Halpern, and B. E. Bouma, "Quantification of macrophage content in atherosclerotic plaques by optical coherence tomography," Circulation **107,** 113-119 (2003).
24. B. E. Bouma, G. J. Tearney, H. Yabushita, M. Shishkov, C. R. Kauffman, D. DeJoseph Gauthier, B. D. MacNeill, S. L. Houser, H. T. Aretz, E. F. Halpern, and I. K. Jang, "Evaluation of intracoronary stenting by intravascular optical coherence tomography," Heart **89,** 317-321 (2003).

1. Introduction

Over the last few decades there has been a continuing search for a high-resolution imaging modality that can quickly and accurately measure the optical properties of layered tissue *in vivo*. Here, the optical properties of interest are those that primarily guide light transport inside the tissue, namely, the scattering coefficient μ_s and anisotropy factor g [1]. A valid method with which these measurements can be done have many important biomedical implications, such as identifying vulnerable atheromatous lesions during percutaneous coronary interventions [2] or distinguishing a tumor from the surrounding healthy tissue for photodynamic treatment [3].

Optical coherence tomography (OCT) is an imaging technology measuring the backscattering properties of tissues [4]. In OCT, the light reflected off a sample is interfered with a reference wave utilizing a technique known as low-coherence interferometry. An interference signal can only arise when the optical pathlength difference between the two arms of a Michelson interferometer is within the coherence length of the source. Thus, the axial resolution in OCT is proportional to the temporal coherence length of the source, and

#3365 - $15.00 US Received 14 November 2003; revised 30 December 2003; accepted 8 January 2004

with a broadband source it is possible to obtain a resolution as high as 0.5 μm in tissue [5]. As a fiber-based technology, OCT can be readily integrated into many catheter-based endoscopic applications [6].

OCT signals are mainly influenced by the scattering properties of the examined sample, i.e., μ_s and g. These are macroscopic physical properties unique to the tissue, which play a vital role in the modeling of OCT signals. By properly modeling an OCT signal as a function of depth so that multiple scattering events are included, and fitting the depth profile of coherent backscattered light in an OCT image (also called depth-scan or A-scan) to such model, it is possible to extract out both μ_s and g. Preliminary clinical investigations [7-10] indicated that additional diagnostic information based on the optical properties could be extracted from OCT images, although the model in Refs. [7,10] considered the single-scattering case only, where only one parameter can be extracted. Reference [7] describes the basic steps necessary to include multiple-scattering effects in the modeling, which would result in fitting two parameters instead of one, as in Refs. [8,9]. Still, the model used in Ref. [8] is restricted in its ability to handle complex geometries, which is an inherent advantage of the model used for this study [11]. Additionally, OCT has the important advantage that images can be obtained *in vivo* from which optical properties may be extracted thereby enabling *in situ* assessment of the tissue and/or lesion. This feature, if successfully implemented, holds considerable promise for future clinical utility.

Our objectives in this study were twofold: firstly, to demonstrate that the curve fitting algorithm we employed, which is based on a general theoretical analysis taking into account multiple scattering effects [11], compared well with controlled experimental measurements and theoretical calculations. This evaluation part of the study was conducted on a set of tissue phantoms using integrating sphere measurements to determine optical scattering properties. Secondly, we applied the OCT extraction method on normal and atherosclerotic human aortic samples in a preliminary *ex vivo* study in order to demonstrate that the technique may provide a basis for distinguishing between different tissues by their optical properties.

In the present paper, we first demonstrate how our curve-fitting algorithm can integrate an established theoretical model that includes multiple-scattering effects in the OCT signal [11] with OCT images and hereby quantify the scattering properties of the imaged sample. Next, we show that this technique can accurately determine these parameters by means of the evaluation study. Finally, we present a preliminary *ex vivo* analysis of normal and atherosclerotic human arteries as an example illustrating how this technique may be applied.

2. OCT

2.1 OCT system and measurements

The OCT system used for this study (Fig. 1) employed a broadband source with a center wavelength of 1300 nm (AFC, Inc., model BBS 1310), providing a subsequent axial resolution of ~10 μm in tissue. The sample arm unit consisted of a handheld probe that the user holds in contact with the sample. A computer controlled transverse scanning module and an integrated digital video camera were incorporated into the probe unit. The digital video camera was used to visually assist transverse scanning. In the reference arm, fast scanning was achieved with use of a Fourier domain rapid-scanning optical delay line [12]. An InGaAs (New Focus, Inc., model 2017) detector measured the interference pattern between the two arms of the interferometer. During the first part of the study, an optical circulator between the source and the 50/50 beam splitter was included in the setup, which was also connected to a second detector to allow for dual balanced detection that increased signal-to-noise ratio (SNR) [13]. The electronic signal emerging from the detector was amplified and high-pass filtered. Detection of the interferometric envelope was implemented in hardware using a programmable logic device. Thereafter, the signal was digitized and stored on a computer.

#3365 - $15.00 US Received 14 November 2003; revised 30 December 2003; accepted 8 January 2004

The OCT system was used to capture depth interferometric information from the investigated samples resulting in images with 690 axial (z) pixels (4.16 μm spacing) and 400

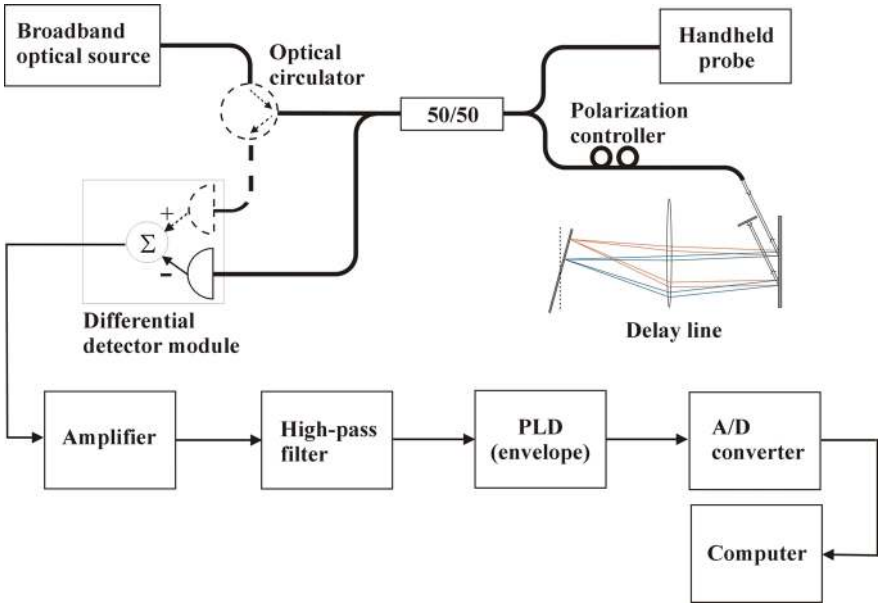

Fig. 1. The OCT system. The optical circulator and a second detector (dashed line) were only used in the first part of the study. PLD: programmable logic device.

transverse (x) pixels (10 μm spacing). In all the images, light was focused on the surface of the scattering medium. Corresponding digital photographs of the sample and the scanned region were automatically taken along with every OCT image. Image acquisition time from start of scanning was 5-6 seconds. The dynamic range of the system was >100 dB.

2.2 OCT Model

A model that analyzes the heterodyne OCT signal as a function of depth has been developed by Thrane et al [11]. Based on the extended Huygens-Fresnel principle [14], this model takes into account multiple scattering effects, and thus the depth profile of the OCT signal is a function of both μ_s and g as well as other parameters. This model is general and capable of handling different sample arm geometries, i.e., dynamic vs. fixed focusing. Furthermore, it is based on ABCD matrix formalism [15], and may therefore easily be applied to a multiple-layered geometry of scattering media, such as is frequently the case with tissue.

As detailed in Ref. [11], the mean square of the heterodyne signal current $\langle i^2(z)\rangle$ at probing depth z measured by an OCT system is a product of two factors, i.e., $\langle i^2(z)\rangle=\langle i^2\rangle_0\Psi(z)$. Here $\langle i^2\rangle_0$ is the mean square heterodyne signal current in the absence of scattering and $\Psi(z)$ is the heterodyne efficiency factor describing the signal degradation due to the scattering. The factor $\langle i^2\rangle_0$ is defined as $\langle i^2\rangle_0=\alpha^2 P_R P_S \sigma_b/\pi w_H^2$ with α being the power to current conversion factor, P_R and P_S the power of the reference and input sample arm beams, σ_b the effective backscattering cross-section, and w_H the 1/e irradiance radius at the probing depth in the absence of scattering, respectively. More precisely, w_H is defined as [11]:

$$w_H^2 = w_0^2\left(A-\frac{B}{f}\right)^2+\left(\frac{B}{kw_0}\right)^2, \qquad (1)$$

where A and B are elements from the ABCD ray-matrix for light propagation from the lens plane to the probing depth in the sample. For the case where the focal plane of the sample beam is fixed on the surface of the sample, A=1 and B=f+z/n. The quantity w_0 represents the

#3365 - $15.00 US Received 14 November 2003; revised 30 December 2003; accepted 8 January 2004

1/e irradiance radius of the input sample beam at the lens plane, $k=2\pi/\lambda$ where λ is the center wavelength of the source, f is the focal length of the lens, and n is the mean index of refraction of the sample.

The factor of interest in the above equation for $\langle i^2(z)\rangle$ is the heterodyne efficiency factor $\Psi(z)$, which contains the scattering effects. Specifically, it has been shown [11] that

$$\Psi(z) = \exp(-2\mu_s z) + \frac{4\exp(-\mu_s z)\left[1-\exp(-\mu_s z)\right]}{1+{w_S}^2/{w_H}^2} + \left[1-\exp(-\mu_s z)\right]^2 \frac{{w_H}^2}{{w_S}^2}. \quad (2)$$

The first term in Eq. (2) represents the single scattering contribution, the third term represents the contribution from multiple scattering events, while the second term is the cross-term. Also, w_S is the 1/e irradiance radius at the probing depth in the presence of scattering [11], that is,

$${w_S}^2 = {w_0}^2\left(A-\frac{B}{f}\right)^2 + \left(\frac{B}{kw_0}\right)^2 + \left(\frac{2B}{k\rho_0(z)}\right)^2, \quad (3)$$

with $\rho_0(z)$ being the lateral coherence length. A derivation of $\rho_0(z)$ [11,16] shows that

$$\rho_0(z) = \sqrt{\frac{3}{\mu_s z}}\,\frac{\lambda}{\pi\theta_{rms}}\left(\frac{nB}{z}\right), \quad (4)$$

where θ_{rms} represents the root-mean-square scattering angle, defined as the half-width at e^{-1} maximum of a Gaussian curve fit to the main frontal lobe of the scattering phase function [17]. As multiple-scattering effects play an important role in the OCT signal in this model [11], a second parameter, θ_{rms}, may also be fitted. The above four equations constitute the model used in our fitting algorithm. It should be pointed out that the calculation of the OCT signal was carried out from closed-form expressions, which is another major advantage of the new algorithm: the measured depth-profile may be fitted to a closed-form expression, thereby reducing computational burden.

Of note, the anisotropy factor g in the model used in this investigation is defined slightly differently than the mean value of the cosine of the deflection angle ($g=\langle\cos\theta\rangle$) [1]. Instead, the model [11] uses the effective anisotropy factor, $g_{eff}=\cos\theta_{rms}$. Typically, $g_{eff} \geq g$. As a result of this, the g value obtained from experimental measurements with the integrating sphere cannot be directly compared to the g_{eff} extracted from OCT images. Instead, the extracted g_{eff} was compared to $\cos\theta_{rms}$ as derived from a Mie calculation of the scattering phase function [1].

2.3 Extraction algorithm

We have developed an algorithm based on Eqs. (1-4) consisting of a set of Matlab codes for the purpose of these analyses. The principles of how optical scattering properties are evaluated from a given image are illustrated in Fig. 2. Fig. 2(A) shows a detailed geometry of the sample arm unit during measurements, and Fig. 2(B) presents a typical raw OCT image of a tissue phantom. First, the user selected a transverse region of interest (ROI, orange dashed inset in Fig. 2(B)) from a given image, consisting of several adjacent depth-scans. These adjacent A-scans were averaged along the lateral direction and linear smoothing was applied using a 5-pixel kernel. This yielded a smoothed, averaged curve with a high SNR that is given in Fig. 2(C). The number of longitudinal pixels to which the model would be fit to was chosen from this curve (magenta dashed inset in Fig. 2(C)). Pixels near the interface between the scattering and non-scattering media (immediately to the left of the inset in Fig. 2(C)) representing a specular reflection were excluded from the fit. At this point, initial value guesses for μ_s and θ_{rms} were entered by the user. Finally, Fig. 2(D) shows a comparison of

#3365 - $15.00 US Received 14 November 2003; revised 30 December 2003; accepted 8 January 2004

data points fit to $\sqrt{\langle i^2(z)\rangle}$, returned along with the scattering coefficient μ_s, the root-mean-square scattering angle, θ_{rms} (g_{eff} =cos θ_{rms}), and error estimates.

Of note, the mean square heterodyne signal current $\langle i^2\rangle_0$, which is proportional to the effective back-scattering cross section σ_b, is also fitted in our algorithm. Assuming an absolute measurement of the OCT signal, σ_b could be extracted. This is, however, often cumbersome in practice. As μ_s and g are representatives of the shape of the OCT signal as a function of depth, these two parameters adequately describe the tissue. Also noteworthy is that the scattering cross-section and the effective back-scattering cross-section are linked through $\sigma_b=\sigma_s(180°)$ and the cross-sections are related to their corresponding coefficients through the density of scattering particles [1]. Finally, we have chosen to fit μ_s instead of μ_b since these values are readily available in the literature for many different tissues.

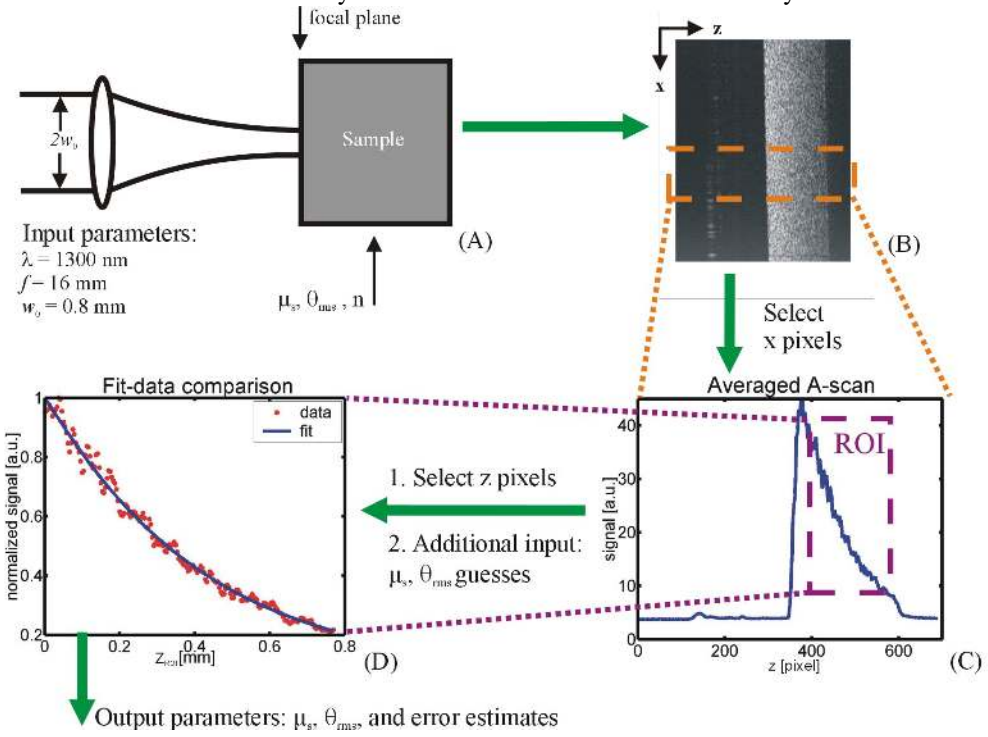

Fig. 2. A schematic representation of the principles of the extraction algorithm. The sample arm geometry and input parameter values from our OCT setup are shown in (A). These parameters were used to generate an image (B) and were also employed during curve fitting (C-D). A transverse ROI was selected in (B, inset), averaged, smoothed, and plotted in (C). The axial pixels of the ROI were chosen in (C, inset), and shown as points in (D). z_{ROI} represents the probing depth within the region of interest in (D). The fit was performed on the resulting data-points using μ_s and θ_{rms} initial value guesses as additional input. The algorithm returned μ_s, θ_{rms}, the fit's error estimates, and a plot comparing the fit to the data points (D).

3. Evaluation study

In order to establish the reliability of our new algorithm for extracting optical properties of highly scattering media, experiments on tissue phantoms with well-controlled optical properties were carried out. Specifically, this verification involved several phantoms with different scattering properties measured with a well-established method for obtaining optical properties from such samples, i.e., the integrating sphere method and inverse adding-doubling (IAD) [18]. To adequately compare the extracted g_{eff} values, the scattering phase function of 1300 nm light in those phantoms was calculated using basic principles from Mie theory [1].

#3365 - $15.00 US Received 14 November 2003; revised 30 December 2003; accepted 8 January 2004

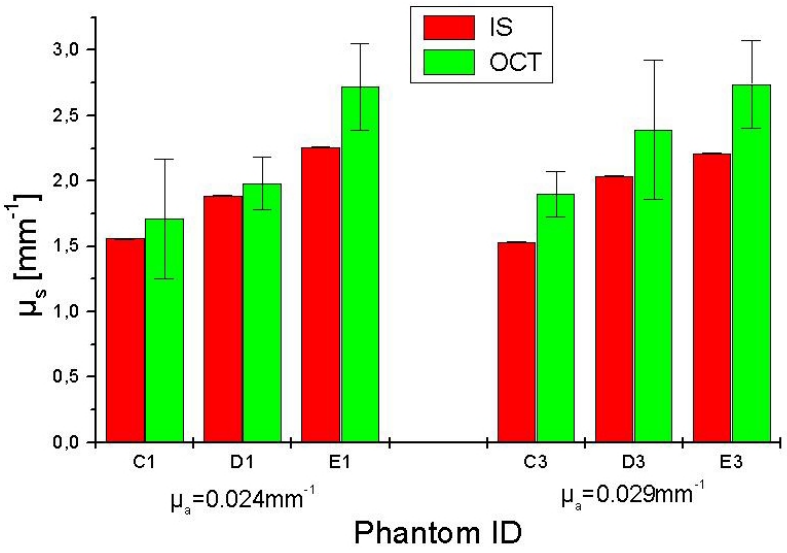

Fig. 3. A comparison of μ_s values (means ± standard deviation) obtained from measurements on tissue phantoms with OCT extractions (green) and the integrating sphere (IS, in red). Note a step wise increase on two separate sets of 3 phantoms purposely prepared to exhibit such an increase. Details about phantom nomenclature can be found in Ref. [19].

3.1 Phantoms

For these experiments, we used six phantoms from a previous investigation [19] with three distinct values of μ_s and two distinct values of absorption coefficient μ_a, respectively. The phantoms consisted of epoxy resin (n=1.55) with well-defined quantities of scattering material and absorbing pigment added for scattering and absorption purposes, respectively. Titanium IV Oxide (TiO_2, n=2.55) powder, with a particle size of 1 μm (Sigma-Aldrich) was used as a scattering material and toner from the photocopying machine served as the absorbing pigment. In all phantoms used, it was ensured that absorption effects were negligible compared to those from scattering. Mounting the phantoms in a slab geometry was achieved by sandwiching 1 ml of each phantom between two microscope slides before the epoxy hardened yielding 1.0 mm thick samples with a cross section measuring 3 x 3 cm^2 [19].

3.2 Integrating sphere measurements

Our measurements of the diffuse reflectance and transmittance were performed using an integrating sphere (Labsphere model RT-060-SF) with the broadband source (AFC) operating at a center wavelength of 1300 nm also used for OCT imaging. Light was guided to the sphere using a single-mode optical fiber and collected by an IR detector supplied by the sphere manufacturer. The beam arriving at the transmission port was 2.3 mm in diameter, with a port diameter of 25.4 mm. A chopper rotating at 730 Hz modulated the beam, and was synchronized with a lock-in amplifier on the detector side to increase SNR. Both diffuse reflectance and diffuse transmittance measurements were done three times each with sample orientation randomized. Our integrating sphere data was processed in version 1 of the inverse adding-doubling (IAD) code [18] using four fluxes per iteration.

3.3 Fitting routine

Each phantom was imaged twice. Based on experience, the true scattering parameters of a phantom are most accurately and reliably determined by performing multiple fits with different sets of input parameters (Fig. 2(C-D)) in each. Specifically, ROIs from different

#3365 - $15.00 US Received 14 November 2003; revised 30 December 2003; accepted 8 January 2004

areas of the image need to be evaluated using various sets of initial value guesses for μ_s and θ_{rms} for each ROI. Also, the number of z pixels in an ROI should be maximized and kept constant. As a consequence of this, the OCT data was evaluated in the following manner: In every image there were five ROIs with fifteen curve fitting attempts per ROI. Curve fitting attempts in a single ROI only differed by the combinations of μ_s and θ_{rms} guesses used. A random number generator determined the transverse boundary pixels for each ROI. The fitted length was chosen to be 0.77 mm (186 pixels), the maximum that could be used in all the images accounting for phantoms imaged at a small angle. Phantoms whose optical depth (i.e., $\mu_s \times$ scattering layer thickness) did not exceed 1.3 as determined with the integrating sphere and thus did not definitively enter the multiple-scattering regime were excluded.

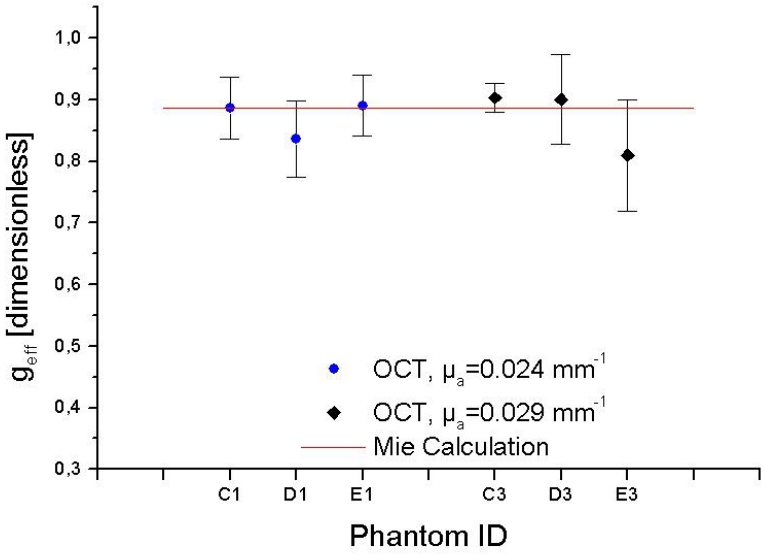

Fig. 4. A comparison of g_{eff} value (means ± standard deviations) from OCT extractions (points) and the Mie calculation (line). Overlap in results is seen for every phantom. Details regarding phantom nomenclature can be found in Ref. [19].

3.4 Results and discussion

A graphical comparison of μ_s obtained from OCT extractions and from the IAD code is shown in Fig. 3. Error bars representing the standard deviation on the measurements are not readily visible on the sphere data since the standard deviation did not exceed 0.25% of the mean. A Mie calculation using the code from Bohren & Huffman for homogeneously shaped spherical particles [1] was performed to obtain a theoretical g_{eff}=0.885. A comparison of g_{eff} derived from OCT extractions to the theoretical result is shown in Fig. 4.

As shown in Figs. 3 and 4, the extraction algorithm generated consistent and reliable results for the tissue phantoms investigated. Every value of g_{eff} extracted overlapped with the 0.885 obtained from the Mie calculation within the error bars (Fig. 4). Moreover, a step-wise increase in μ_s was clearly observed with two different phantom sets (3 phantoms/set) using *both* techniques. While the error bars in three of six phantoms overlapped with the value returned from the IAD algorithm, the difference in the remaining three did not exceed 13% of the IAD returned value. One can notice, however, that the OCT-technique seems to slightly overestimate the scattering coefficient for these particular samples.

In examining the potential sources of error in the OCT extractions, the following should be considered: The integrating sphere measures optical properties of scattering media on a macroscopic scale as an average throughout the sample, while optical property extractions

#3365 - $15.00 US Received 14 November 2003; revised 30 December 2003; accepted 8 January 2004

from an OCT image involves averaging over a much smaller region. Thus, inevitable phantom inhomogeneities on a μm scale could have affected our results. Also, IAD does not take wavelength as one of its inputs [18], or in other words, is designed for monochromatic light where samples exhibit uniform optical properties. The source used in this experiment had a 3 dB bandwidth of 60 nm, which could have an influence on the experiments and thus the returned IAD data. Furthermore, phantom albedos (~0.97) were slightly outside the recommended range of 0.4-0.95 for achieving the highest accuracy with the IAD algorithm [20], and this too could have slightly offset the IAD data points.

Considering the fine overall agreement between extracted values using our new algorithm and the IAD algorithm, we conclude that our new algorithm is capable of extracting optical properties with sufficient reliability.

4. Preliminary *ex vivo* study

Recently, OCT has shown promise for imaging of coronary atherosclerotic plaques [21-24]. At present, however, visual differentiation between the general histopathological types of plaques, i.e., fibrous, fibrocalcific, and lipid-rich lesions, in OCT images is inherently qualitative and subjective. Several features of atherosclerotic plaque histopathology, i.e., reorganization and disruption of intimal collagen fibers, are expected to produce marked changes in the tissue optical scattering properties (μ_s and g_{eff}). Thus, to exemplify how our OCT algorithm may provide quantitative information about complex tissue pathology, we performed a preliminary *ex vivo* investigation in human atherosclerotic lesions.

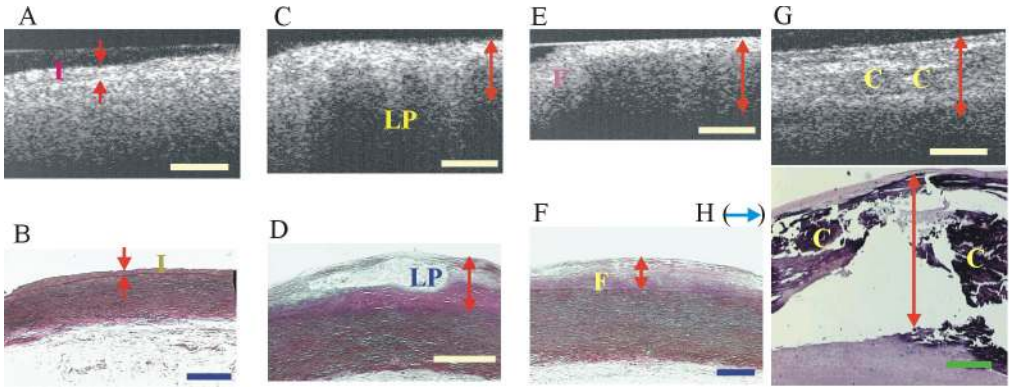

Fig. 5. Correlation of raw OCT images (A, C, E, and G) and histopathology (B, D, F, and H). Normal intima labeled 'I' in (A-B). Lipid-rich lesion (C-D), with a lipid pool marked 'LP'. Fibrous plaque (E-F), with fibrous area marked 'F'. Fibrocalcific lesion (G-H), with the calcifications denoted 'C'. Rupture artifacts caused by the decalcifying process are clearly seen in (H). The arrows represent the intima in (A-F) and the fitting region in (G-H), respectively. Bars=500 μm.

4.1 Curve fitting and imaging

Fourteen (4 normal, 4 lipid-rich, 3 fibrous, and 3 fibrocalcific) aortic segments were obtained within four hours of autopsy and imaged with OCT in phosphate buffered saline. During OCT imaging, the OCT probe was in contact with a glass cuvette inside of which the biopsies were mounted. Regions corresponding to those imaged by OCT were marked and located on digital photos. The samples were routinely paraffin embedded and sliced at the regions defined by the digital photographs. Sections were stained (hematoxylin and eosin or combined elastin and van Gieson Hansen staining) and corresponding areas of the intima were identified in OCT images and histological sections, respectively, using Table 1 in Ref. [21] as a guide. The OCT images were laterally divided into ROIs spanning approximately 20-30 A-scans or 200-300 μm. Altogether, the images were subdivided into 151 ROIs, including 41 normal, 40 lipid-rich, 34 fibrous, and 36 fibrocalcific ROIs, with each ROI being

#3365 - $15.00 US Received 14 November 2003; revised 30 December 2003; accepted 8 January 2004

systematically selected for the criterion of the ROI spanning an area with uniform scattering properties. To facilitate interpretation, the extracted data were grouped into intervals based on the respective values of μ_s and g_{eff}. For μ_s, the intervals spanned 5 mm^{-1} for values from 0 to 40 mm^{-1}, and 10 mm^{-1} for values over 40 mm^{-1}. Since human soft tissue is generally very forward scattering, g_{eff} range intervals of 0.05 were chosen for g_{eff} values near 1, but the interval range was larger for the limited number of g_{eff} values below 0.8.

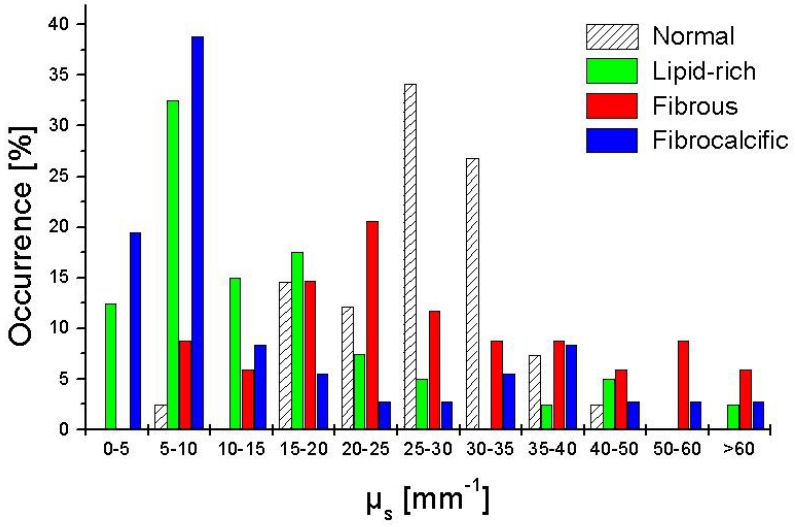

(A)

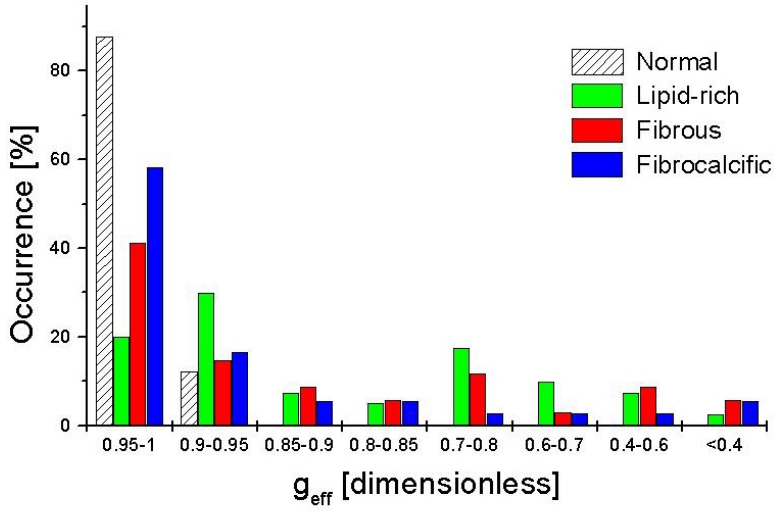

(B)

Fig. 6. Distributions of μ_s (A) and g_{eff} (B) for normal arteries and lipid-rich, fibrous, and fibrocalcific atherosclerotic plaques, respectively. In (A), μ_s for normal samples (striped) were centered between 15 and 40 mm^{-1}, but were centered at lower values for lipid-rich (green) and fibrocalcific (blue) plaques, and were randomly distributed for fibrous plaques (red). In (B), g_{eff} values were generally higher in normal intimas than in atherosclerotic lesions.

#3365 - $15.00 US Received 14 November 2003; revised 30 December 2003; accepted 8 January 2004

4.2 Initial results

OCT images were correlated with the corresponding histological sections using Table 1 in Ref. [21] as a guide and representative samples are shown in Fig. 5. Qualitatively, images obtained by OCT and microscopy demonstrated similar gross histopathological features that allowed for reasonable differentiation between normal vessels and lipid-rich, fibrous, and fibrocalcific plaques, respectively. The distribution of μ_s and g_{eff} for ROIs of normal arteries and the three overall atherosclerotic lesion types is shown in Fig. 6. Our preliminary data suggested that very similar optical properties were observed in images of normal samples (diagonal lines) but not in those representing atherosclerotic lesions. In normal arteries, almost 90% of g_{eff} values were concentrated between 0.95 and 1, whereas more than 50% of atherosclerotic lesion ROIs were below 0.95. Approximately 95% of the normal arterial samples had μ_s between 15 and 39 mm^{-1}, while μ_s was below 15 mm^{-1} in about 60% of lipid-rich and fibrocalcific plaques. Furthermore, fibrous lesions demonstrated very considerable variations in μ_s.

To our knowledge, the above preliminary data represent the first quantitative analysis of the optical scattering properties, i.e., the scattering coefficient and the anisotropy factor, of the normal and diseased human aortic intima *in vitro* at 1300 nm. The study indicates that the presented algorithm may provide a basis for extension of the OCT technique beyond qualitative image assessment towards tissue characterization based on physical principles. Techniques for detection of unstable atherosclerotic lesions have generated enormous interest in the field of vascular biology, and the future clinical utility of such methods is dependent on minimizing subjective and operator-dependent bias in the acquisition and interpretation of data [2]. We therefore suggest that the current OCT algorithm is an important step in this direction and that further studies are warranted to define the validity of the described method for characterization of atherosclerotic lesions.

5. Conclusion

The current study demonstrated that with use of the outlined algorithm, the optical scattering properties of tissue may be obtained from optical coherence tomography images. The evaluation study on phantoms showed that OCT is capable of accurately determining the optical scattering properties, i.e., the scattering coefficient μ_s and effective anisotropy parameter g_{eff}, of highly scattering media, obtaining results in agreement with a well-established experimental method. Using this technique, we were able for the first time to conduct a preliminary investigation that quantitatively compared the optical scattering properties of the human arterial intima *ex vivo*. Furthermore, our preliminary *ex vivo* tissue data indicated that differences in scattering properties data may exist between normal and atherosclerotic arterial segments and that optical scattering data provided by OCT can potentially contribute to plaque characterization. The OCT technique presented here opens many new avenues of research combining high-resolution tissue visualization and scattering properties measurements. This may allow for the assessment of yet unexplored biophysical properties of tissues and holds considerable promise for future clinical utility.

Acknowledgments

The authors would like to thank the staff at the Department of Pathology, Rigshospitalet, Denmark, for inviting us and for providing the aortic biopsies for imaging. We also want to thank Andreas Tycho of OCT Innovation ApS., and Finn Pedersen of Risø National Laboratory for helping with the imaging and sample handling. This work was financially supported by the Danish Technical Research Council, grant number 9901433, the BIOP graduate school, and the Danish Heart Foundation.

#3365 - $15.00 US Received 14 November 2003; revised 30 December 2003; accepted 8 January 2004